Double-Zero-Index Structural Phononic Waveguides

Hongfei Zhu and Fabio Semperlotti

Phys. Rev. Applied **8**, 064031 — Published 29 December 2017

DOI: 10.1103/PhysRevApplied.8.064031

Double-zero-index structural phononic waveguides

Hongfei Zhu[1, 2, *] and Fabio Semperlotti[2, †]
[1] Department of Aerospace and Mechanical Engineering, University of Notre Dame, Notre Dame, IN 46556, USA
[2] Ray W. Herrick Laboratories, School of Mechanical Engineering, Purdue University, West Lafayette, Indiana 47907, USA
(Dated: December 5, 2017)

We report on the theoretical and experimental realization of a double-zero-index elastic waveguide and on the corresponding acoustic cloacking and supercoupling effects. The proposed waveguide uses geometric tapers in order to induce Dirac-like cones at $\vec{k} = 0$ due to accidental degeneracy. The nature of the degeneracy is explored by a $k \cdot p$ perturbation method adapted to thin structural waveguides. Results confirm the linear nature of the dispersion around the degeneracy and the possibility to map the material to effective medium properties. Effective parameters, numerically extracted using boundary medium theory, confirm that the phononic waveguide maps into a double zero index material. Numerical and experimental results confirm the expected cloacking and supercoupling effects.

I. INTRODUCTION

The concept of acoustic metamaterials [1, 2] has rapidly emerged as a powerful alternative to design materials and structures exhibiting unexpected dynamic properties typically not achievable in natural materials. The early development of the concept of metamaterials dates back to 1968 when Veselago [3] predicted materials exhibiting simultaneously negative permeability and permittivity. Such negative index media remained substantially unexploited until, almost thirty years later, Pendry [4] suggested the possibility to achieve the amplification of evanescent waves, which would have profound effects on lens design and imaging applications. The first experimental observation of negative index materials was provided shortly afterwards by Smith [5, 6] who designed a periodic array of interspaced conducting and non-magnetic split ring resonators. Following these pioneering studies, the scientific community has rapidly extended the underlying physical concepts to other fields of classical mechanics such as acoustics and elastodynamics. In less than two decades, this concept has allowed a drastic expansion of the material design space enabling novel applications involving acoustic wave management and control. Properties such as acoustic bandgaps [7–12], focusing [13–17], collimation [18–20], sub-wavelength resolution [21–26], and negative refraction [27–30], have been discovered and studied in depth. More recently, researchers have shown a rather new and exciting property of these materials consisting in their ability to achieve near-zero effective parameters. This class of materials was first formulated for electromagnetic waves where epsilon-near-zero (ENZ), mu-near-zero (MNZ), and epsilon-and-mu-near-zero (EMNZ) properties were first obtained. Applications included antenna designs with high directivity [31, 32] and enhanced radiation efficiency [33, 34], as well as the realization of unconventional tunneling of electromagnetic energy within ultra-thin subwavelength channels or bends [35–37]. Among the most peculiar characteristics of these materials, we mention the independence of the phase from the propagation distance. This means that a wave entering a double-zero-index material emerges on the other side having the exact same phase as the input. In addition, double-zero materials are also characterized by a high level of transmissibility, ideally acting as a non-reflective waveguide even in presence of sharp impedance discontinuities.

In analogy with a EMNZ, an acoustic double-zero-index material (DZIM) corresponds to a medium with simultaneous zero effective mass density and elastic compliance. While materials with near-zero permittivity are available in nature (e.g. some noble metals, doped semiconductors [38], polar dielectrics [39], transparent conducting oxide (TCOs) [40]), in acoustics near-zero density and elastic compliance must be achieved via effective quantities by leveraging the local dynamic response of the medium. In the past few years, some acoustic metamaterials were reported to exhibit single zero effective parameters, such as near zero density [41–43]. We note that this behavior is the exact counterpart to single zero electromagnetic materials, such as the ENZ. Although these materials offered good control on the phase, they suffered from low-transmissibility due to an intrinsic impedance mismatch between the host and the zero effective density medium. Double-zero materials target specifically this limitation of the transmission properties. However, designing acoustic media with double-zero effective properties is not a trivial task given that they are not readily available in nature.

Recent studies on photonic and phononic crystals [44–50] revealed that when a Dirac-like Cone (DC) can be obtained at the center of the Brillouin zone, such lattice can be mapped into a double-zero refractive index material. This observation has drastically extended the possibility to design materials having near-zero effective properties. Nevertheless, while different applications of this

* Hongfei.Zhu.44@nd.edu
† To whom correspondence should be addressed: fsemperl@purdue.edu

basic concept were explored in photonics and phononics, there has been very little research targeting the implementation of these effective material properties in solids [44, 51]. The research on elastic phononic waveguides has been lagging behind even more and it currently counts no attempt of designing zero-index properties. In addition, the experimental implementation and validation of zero-index elastic media has not been reported in the scientific literature mostly due to the complexities associated with their design and fabrication.

In the present study, we report on the theoretical, numerical, and experimental realization of a structural phononic waveguide exhibiting double-zero-index behavior and capable of achieving acoustic cloaking and supercoupling. The proposed design builds upon a class of metamaterials recently introduced by the authors [52–54] and based on geometric tapers realized in a single-material system. The specific design employed in this study can be thought as an equivalent locally-resonant unit where an internal resonating core is embedded within a more compliant medium (i.e. the taper). Geometrically tapered metamaterials [52] exhibit Dirac-like Cones (DC) at the center of the Brillouin zone (Γ point) that are the result of accidental degeneracies [55]. In other terms, the degeneracy is induced by the specific combination of the geometric parameters of the tapers and it is not protected by the underlying lattice structure (like, for example, in graphene). The bands emanating from the three-fold degenerate point (the Dirac-like point) exhibit isotropic linear dispersion. We will show that these properties are the foundation that allows achieving double-zero effective properties in this class of materials. In particular, we will show that in the neighborhood of this degenerate point our waveguide exhibits simultaneous zero mass density and zero reciprocal shear modulus (or, equivalently, infinite shear modulus or zero elastic compliance in shear).

Possible applications of such materials may include, but are not limited to, efficient energy transmission across discontinuities (e.g. joints in thin-walled structures) and consequent reduction of localization effects and dynamic amplification, efficient energy extraction for dissipation and/or harvesting regardless of the location or the spatial distribution of the acoustic source, and vibration isolation of sensitive components. We anticipate the proposed DZIM design to be virtually scalable to any frequency range and geometric dimensions. In the case of lightweight structural applications, such as those involved in many transportation systems, the typical dimensions of the unit cell would range between 2 and 6 mm in thickness and 1 to 4 cm in terms of lattice constant. Such dimensions would allow elastic wave control via DZIM properties in a frequency range of approximately 20 to 100 kHz (considering aluminum alloys). Equivalently, the wavelength will range between 6 to 1.5 cm. In more general terms, a straightforward approach to rescale the proposed design in order to operate at a different frequencies consists in isotropically rescaling the dimensions and the dispersion properties by keeping $\lambda/L = constant$, where L is the lattice constant and λ is the wavelength at a frequency f. As an example, dividing all the geometric dimensions by a factor of 2 will double the operating frequency. This approach would allow a simple rescaling without requiring a complete redesign of the unit. It is foreseeable that the DZIM design could be implemented also at the microscales. Many applications in the telecommunications area exploit analog filtering of surface acoustic waves as an integral part of their modulation/demodulation systems. DZIM-based filters could open new possibilities to carefully tailor the transfer function of these systems. The rescaling argument discussed above suggests that at the sub-millimiter scales the design will experience a substantial increase in the operating frequencies that would likely belong to the low MHz range while transitioning to the high MHz range for dimensions on the order of microns. From a fabrication perspective, it is expected that currently available additive manufacturing techniques already allow sufficient precision to build such materials.

II. RESULTS

A. Double-zero index waveguide via geometric tailoring

The proposed phononic waveguide employs a tapered unit cell in a square lattice configuration (C_{4v} symmetry). The unit cell consists of a square plate having an embedded elliptic torus-like taper and a (resonating) center mass. The unit is also symmetric with respect to the mid-plane of the waveguide (Fig.1). The $x-z$ cross-section of the unit is shown in Fig.1b and shows the main geometric parameters where t is the thickness of the element, L is the lattice constant, a and b are the lengths of the minor and major axes of the ellipse, r is the radius of the torus, and h is the thickness of center mass. The unit was made out of aluminum with mass density $\rho = 2700$ kg/m^3, Young's modulus $E = 70$ GPa, and the Poisson's ratio $\nu = 0.33$.

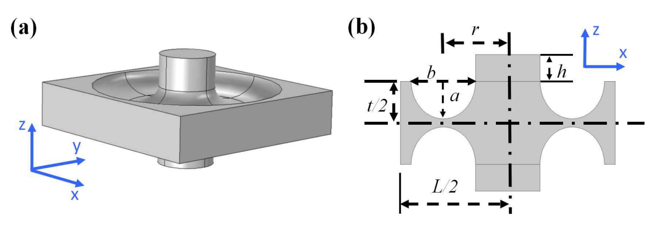

FIG. 1. Schematic of (a) the fundamental tapered unit cell, and (b) its $x-z$ cross-section showing the main geometric parameters. The tapered geometry is symmetric with respect to the mid-plane of the plate.

The dispersion relations for the proposed system were calculated using a commercial finite element solver (Comsol Multiphysics). Given the finite dimension of the unit cell in the thickness direction the dispersion curves are composed by symmetric (S), anti-symmetric (A), and

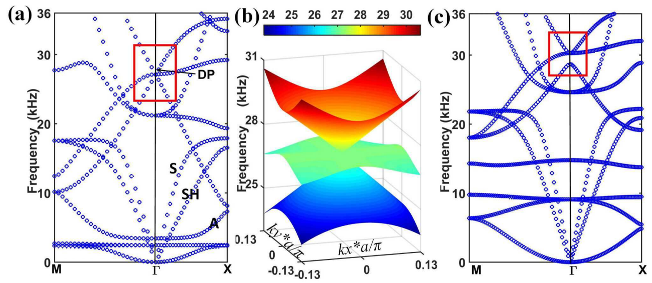

FIG. 2. (a) The dispersion relations around $f = 27.02$ kHz showing the existence of a triple-degenerate point and a Dirac-like cone (red box) for a given selection of the taper parameters. (b) Equi-Frequency-Surface plot corresponding to the frequency range around the DP and showing the formation of the Dirac-like cones. (c) When the geometric configuration is slightly perturbed (taper coefficient a changed from 0.0039 to 0.0035) the Dirac-like cone opens up, confirming that the formation of the linear dispersions is due to an accidental degeneracy.

shear horizontal (SH) guided Lamb modes. By using a proper selection of the geometric parameters (specifically $L = 0.04$m, $t = 0.008$m, $a = 0.0039$m, $b = 0.007442$m, $r = 0.012$m and $h = 0.013$m), the band structure of the waveguide was tuned to exhibit a three-fold degenerate point (the Dirac-like Point, DP) at $f = 27.04$ kHz and $\vec{k} = 0$ (Fig.2a). Note that the branches emanating from the degenerate point are isotropic and linear, and form two cones touching on their vertices at the DP (Fig. 2b). The cones are made of A_0 modes having non-zero but constant group velocity and are intersected by an A_0 flat band at the DP.

The Dirac-like cone is the result of an accidental degeneracy, which can be confirmed by slightly perturbing the geometric parameters. By perturbing the torus-like taper a (from 0.0039 to 0.0035) the cones separate (Fig.2c) and the triple degenerate point splits into a non-degenerate and a doubly degenerate band. The corresponding eigenstates of the three degenerate modes are provided in Fig.4a which shows, from top to bottom, the lower cone, the flat band, and the upper cone.

B. Analysis of the Dirac-like cones

To further understand the origin of the Dirac-like dispersion, we extended the $\vec{k}\cdot\vec{p}$ method (well-known in electronic applications[56]) to analyze our phononic system. This method was recently adopted by Mei[55] to analyze the Dirac and Dirac-like cones in two-dimensional phononic (sonic) and photonic crystals.

Our system is described by the Navier's equations with traction-free boundary conditions on the top and bottom surfaces of the waveguide. Imposing such boundary conditions when in presence of tapers creates non-trivial complexities due to the changing direction of the unit vector normal to the tapered surface. To simplify the modeling, we resorted to an approach previously used to extend the three-dimensional plane wave expansion method to 2D phononic waveguides [52, 57]. According to this method, we can view the two-dimensional waveguide as part of a three-dimensional, layered, periodic bulk material constructed by alternating the waveguide with vacuum layers (Fig.3a) along the thickness direction. The vacuum layers have negligible mass density and modulus so to allow for the traction-free boundary conditions on the surface of the waveguide to be automatically satisfied. The three-dimensional periodic medium so obtained, whose unit cell is shown in Fig.3b, can be modeled as a layered bulk material by the Navier's equations and solved in order to extract the dispersion relations. Note that the use of the vacuum layer ensures that the periodic images of the waveguide along the thickness direction are dynamically decoupled from each other, therefore simply resulting in repeated roots in the dispersion calculation. This approach allows an efficient implementation of the adapted $\vec{k}\cdot\vec{p}$ method for bulk elastic systems as presented below.

We can then write the general form of the Navier's equations for an inhomogeneous bulk medium in the vector form as,

$$\begin{aligned} -\rho\omega^2\vec{U} = (\lambda+\mu)\nabla(\nabla\cdot\vec{U}) + \mu\nabla^2\vec{U} + \nabla\lambda\nabla\cdot\vec{U} \\ +\nabla\mu\times\nabla\times\vec{U} + 2(\nabla\mu\cdot\nabla)\vec{U} \end{aligned} \tag{1}$$

here $\vec{U}(\vec{r})$ is the particle displacement vector, $\rho(\vec{r})$ is the local density, $\lambda(\vec{r})$ and $\mu(\vec{r})$ are the local Lamé constants, which are all functions of the spatial variables.

According to Mei [55], we assume that all the Bloch states at the Γ point ($\vec{k_0} = 0$) are known and given by, $\vec{U}_{n0}(\vec{r}) = e^{i\vec{k_0}\cdot\vec{r}}\vec{\psi}_{n0}(\vec{r}) = \vec{\psi}_{n0}(\vec{r})$, as well as the corresponding eigenfrequency ω_{n0}, where "n" denotes the band index. The Bloch states at a generic wave vector $\vec{k}$ near $\vec{k_0} = 0$ can then be written as,

$$\begin{aligned} \vec{U}_{n\vec{k}}(\vec{r}) = \vec{\psi}_{n\vec{k}}(\vec{r})e^{i\vec{k}\cdot\vec{r}} = e^{i\vec{k}\cdot\vec{r}}\sum_j A_{nj}(\vec{k})\vec{\psi}_{j0}(\vec{r}) \\ = \sum_j A_{nj}(\vec{k})e^{i(\vec{k}-\vec{k_0})\cdot\vec{r}}\vec{U}_{j0}(\vec{r}) = \sum_j A_{nj}(\vec{k})e^{i\vec{k}\cdot\vec{r}}\vec{U}_{j0}(\vec{r}) \end{aligned} \tag{2}$$

where the unknown periodic functions $\vec{\psi}_{n\vec{k}}(\vec{r})$ have been expressed as a linear combination of the $\vec{\psi}_{j0}(\vec{r})$. Substituting Eqn.(2) into Eqn.(1) and collecting terms linear in $\vec{k}$ we obtain,

$$\begin{aligned} \sum_j A_{nj}(\vec{k})e^{i\vec{k}\cdot\vec{r}} \times \Bigg\{ \rho(\vec{r})(\omega^2_{n\vec{k}} - \omega^2_{j0})\vec{U}_{j0}(\vec{r}) \\ +2\mu(\vec{r})i\vec{k}\cdot[\nabla\vec{U}_{j0}(\vec{r})] + (\lambda(\vec{r})+\mu(\vec{r}))\nabla[i\vec{k}\cdot\vec{U}_{j0}(\vec{r})] \\ +(\lambda(\vec{r})+\mu(\vec{r}))i\vec{k}[\nabla\cdot\vec{U}_{j0}(\vec{r})] \\ +\nabla\lambda(\vec{r})[i\vec{k}\cdot\vec{U}_{j0}(\vec{r})] + \nabla\mu(\vec{r})\times[i\vec{k}\times\vec{U}_{j0}(\vec{r})] \\ +2[\nabla\mu\cdot i\vec{k}]\vec{U}_{j0}(\vec{r}) + o(k^2) \Bigg\} = 0 \end{aligned} \tag{3}$$

Utilizing the orthonormality property of the basis functions $\vec{U}_{j0}(\vec{r})$, i.e. $\frac{(2\pi)^3}{V}\int_{unitcell}\rho(\vec{r})\vec{U}_{j0}(\vec{r})\cdot\vec{U}^*_{l0}(\vec{r})d\vec{r}=\delta_{jl}$, where V is the volume of the unit cell, Eqn.(3) can be written as,

$$\sum_j\left[(\omega^2_{n\vec{k}}-\omega^2_{j0})\delta_{lj}+P_{jl}(\vec{k})\right]A_{nj}(\vec{k})=0 \tag{4}$$

where,

$$P_{jl}(\vec{k})=i\vec{k}\cdot\vec{p}_{jl}(\vec{k}) \tag{5}$$

and up to the first order in $\vec{k}$ we can write,

$$p_{jl}(\vec{k})=\frac{(2\pi)^3}{V}\int_{unitcell}\Big\{(\lambda+\mu)(\nabla\vec{U}_{j0})^T\cdot\vec{U}^*_{l0}+ (\lambda+\mu)[\nabla\cdot\vec{U}_{j0}(\vec{r})]\vec{U}^*_{l0}+2\mu\nabla\vec{U}_{j0}\cdot\vec{U}^*_{l0}+[\nabla\lambda\cdot\vec{U}^*_{l0}]\vec{U}_{j0} +2(\vec{U}_{j0}\cdot\vec{U}^*_{l0})\nabla\mu+[\nabla\mu\cdot\vec{U}_{j0}]\vec{U}^*_{l0}-[\vec{U}_{j0}\cdot\vec{U}^*_{l0}]\nabla\mu\Big\} \tag{6}$$

Eqn.(4) has nontrivial solutions only when the following secular equation is satisfied,

$$det|(\omega^2_{n\vec{k}}-\omega^2_{j0})I+P(\vec{k})|=0 \tag{7}$$

where I is the identity matrix. Since we are interested in the linear dispersions of the Dirac-like cone, we only consider the degenerate states at the Dirac-like point in the summation of Eqn. (2). In fact, other bands only contribute to the higher order terms of $\vec{k}$. For small $\vec{k}$, the analytic solution for Eqn. (7) can be expressed as,

$$\frac{-2\omega_{j0}\Delta\omega}{\Delta k}=\gamma_\beta+o(\Delta k), \qquad \beta=1,2,3 \tag{8}$$

where we approximated the term $\omega^2_{j0}-\omega^2_{n\vec{k}}$ as $-2\omega_{j0}(\Delta\omega)$.

After evaluating Eqn.(6) numerically (detailed expressions of its elements can be found in Appendix), the reduced Hamiltonian matrix for our system is given by,

$$\vec{p}_{jl}=10^8\begin{pmatrix}(0,0) & (0.002,-4.9983) & (-4.9902,-0.002)\\ (-0.002,4.9930) & (0,0) & (0,0)\\ (4.9849,0.002) & (0,0) & (0,0)\end{pmatrix} \tag{9}$$

Note that $\vec{p}_{12}=-\vec{p}_{21}$, $\vec{p}_{13}=-\vec{p}_{31}$, $|p_{12}|=|p_{13}|$ and $\vec{p}_{12}\perp\vec{p}_{13}$; these properties are required to guarantee the isotropy of the cones. By substituting Eqn.(9) into Eqn.(7), we get the dispersion relations of the modes contributing to the Dirac-like cone,

$$\begin{aligned}\frac{\Delta f}{\Delta k}&=0\\ \frac{\Delta f}{\Delta k}&=\pm\frac{|\vec{p}_{12}|}{8\pi^2 f_0}=\pm 233.48\end{aligned} \tag{10}$$

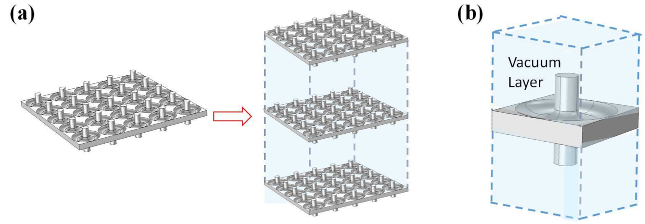

FIG. 3. Schematics of (a) the periodic waveguide and its assembly in a 3D bulk layered medium used to calculate the dispersion relations. (b) detailed view of the unit cell of the 3D bulk periodic medium showing the waveguide unit cell and the vacuum layers.

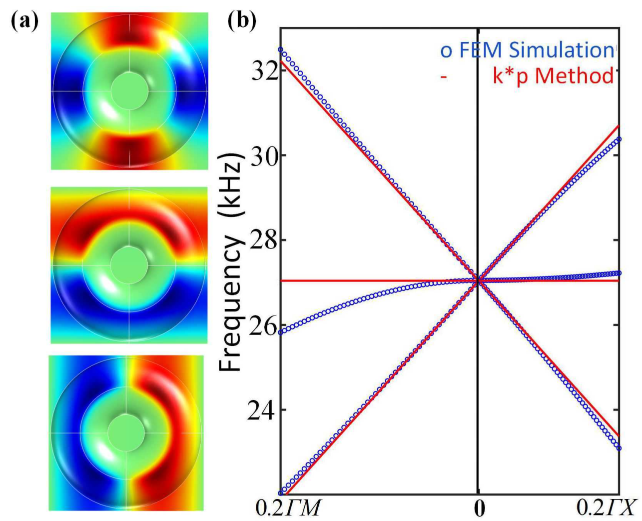

FIG. 4. (a) The eigenstates corresponding to the three degenerate states at the DP. From top to bottom, we find the state of the negative slope band, the flat band, and the positive band. (b) Comparison of the linear dispersion prediction at the DP obtained from the $\vec{k}\cdot\vec{p}$ method and the finite element simulations.

Obviously the first result in Eqn.(10) corresponds to the flat band while the remaining two signed values correspond to the linear dispersion associated with the cones. Note that these results do not depend on the wave vector $\vec{k}$ direction thus confirming the isotropy of the linear dispersion. Equations (10) can be plot together with the numerically obtained dispersion relations (Fig.4b) in order to illustrate the good agreement between the $\vec{k}\cdot\vec{p}$ method and the full field numerical results. It can be seen from Eqn.(6) that the linear slopes γ_β are only determined by the non-diagonal element of the p_{jl} matrix. This term represents the strength of the coupling between the degenerate states, and indicates that the frequency repulsion effect gives rise to the Dirac-like Cones.

C. Effective medium properties

Under certain conditions, the characteristics of the medium around the Dirac-like point can be mapped to effective medium properties. This manipulation allows a very clear characterization of the double-zero properties. Note that, although the selected DP has a relatively high frequency (the wavelength in an equivalent flat plate is about 1.25a), we employed the boundary effective medium theory [58] to obtain the equivalent effective material parameters. It has been argued [59, 60] that, for periodic media, the effective medium theory [61, 62] is still valid at $\vec{k} = \vec{0}$ around the standing wave frequency even when, strictly speaking, the frequency belong to the short wavelength regime. From a more empirical perspective, we will also show that the use of the effective medium description matches well the finite element model predictions, therefore further confirming the validity of the effective medium approach.

The boundary effective medium theory [58] treats the unit cell as a *black-box* that responds to an incoming wave. According to this method, we calculate the eigenstates and then evaluate the modal effective forces, displacements, strains, and stresses from the response collected along the boundaries of the unit cell. The effective density and modulus are then extracted by using the Newton's second law and the constitutive relations.

As an example, for the eigenstates along the ΓX direction, the effective mass density can be obtained from the Newtons second law as,

$$\rho^{eff} = \frac{m^{eff}}{a^2 h} = \frac{F_z^{eff}}{\ddot{u}_z^{eff} a^2 h} = \frac{-F_z^{eff}}{\omega^2 u_z^{eff} a^2 h} \tag{11}$$

where ρ^{eff} is the effective mass density, F_z^{eff} is the effective net force exerted on the unit cell in the out-of-plane Z direction, and u_z^{eff} is the effective displacement of the unit cell in the z direction resulting from the three degenerate states contributing to the Dirac-like Cone. F_z^{eff} and u_z^{eff} can be obtained as,

$$\begin{aligned} F_z^{eff} = & \int T_{xz} dydz \bigg|_{x=a} - \int T_{xz} dydz \bigg|_{x=0} \\ & + \int T_{yz} dxdz \bigg|_{y=a} - \int T_{yz} dxdz \bigg|_{y=0} \end{aligned} \tag{12}$$

and

$$u_z^{eff} = \frac{\int u_z dydz \Big|_{x=a} + \int u_z dydz \Big|_{x=0}}{2ah} \tag{13}$$

Since all the contributing modes are anti-symmetric modes, we only consider the effective shear moduli. They can be obtained from the constitutive relations as follows,

$$\begin{aligned} T_{xz}^{eff} &= G^{eff} S_{xz} \\ T_{yz}^{eff} &= G^{eff} S_{yz} \end{aligned} \tag{14}$$

where G^{eff} is the effective shear modulus, and T^{eff} and S^{eff} are the effective stress and strain tensors. Using the first of Eqn. (14), as an example, the stress and strain can be obtained as,

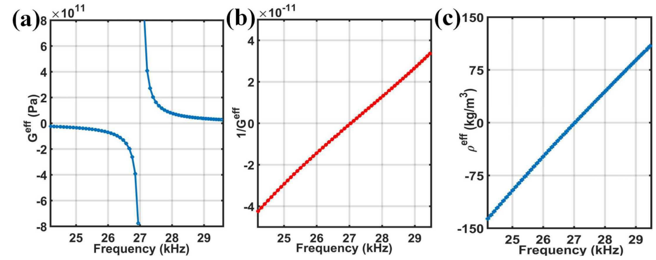

FIG. 5. Frequency dependence of (a) the effective shear modulus G^{eff}, (b) the reciprocal effective shear modulus $1/G^{eff}$, and (c) the effective mass density ρ^{eff} near the Dirac-like point.

$$T_{xz}^{eff} = \frac{\int T_{xz} dydz \Big|_{x=a} + \int T_{xz} dydz \Big|_{x=0}}{2ah} \tag{15}$$

and

$$S_{xz}^{eff} = \frac{\int u_z dydz \Big|_{x=a} - \int u_z dydz \Big|_{x=0}}{a^2 h} \tag{16}$$

Figures 5a and c show the effective shear modulus and the effective mass density as function of frequency in the range around the Dirac-like point. THe results clearly indicate that, below the DP, the proposed metamaterial design behaves as a double negative material while above the DP it behaves as a double positive material. Similarly, the calculation of the reciprocal effective shear modulus (Fig.5b) shows that both ρ^{eff} and $1/G^{eff}$ vary linearly and become zero simultaneously as the frequency crosses the Dirac-like point. These results suggest that the proposed metamaterial should exhibit propagation properties consistent with a double-zero-index material. In particular, we expect that acoustic waves traveling through the medium at the DP frequency should not experience any spatial phase change.

D. Full field numerical analyses

In order to validate the theoretical predictions, we built a numerical model of an elastic waveguide made out of the proposed double-zero-index material. The basic test structure consisted of a flat plate with a 11×12 lattice of torus-like tapers embedded in the center (Fig.6a and b). Both the left and right boundaries were treated with perfectly matched layers (not shown) to avoid reflections, while top and bottom boundaries were treated with periodic boundary conditions in order to simulate an infinite plate. The zero-index material slab was excited from the left by a planar A_0 wave at $f = 27.04$ kHz and normal incidence. The resulting wave field (Fig.6a) indicated that no phase change occurred inside the metamaterial slab and nearly full transmission was achieved due to the zero-refractive-index and the matched impedance with the flat plate. These peculiar transmission properties were tested to show the ability to achieve cloaking and supercoupling in structural waveguides.

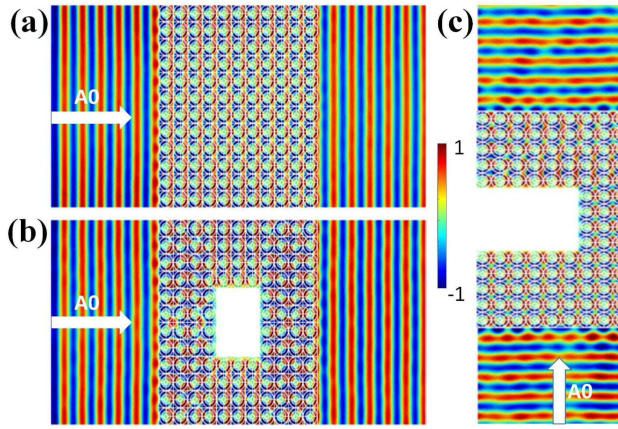

FIG. 6. (a) The out-of-plane displacement distribution of the wave field when an incident A_0 planar wave at $f = 27.04$ kHz impinges normally onto the 11×12 lattice of double-zero-index material. The top and bottom boundaries were treated with periodic boundary conditions while the left and right boundaries used PMLs to avoid reflections. As expected, no phase change occurs inside the metamaterial slab. (b) The out-of-plane displacement field showing the cloaking capability of the double zero material when an object 3×4 units in dimension is embedded in the slab. (c) The out-of-plane displacement field showing the supercoupling capabilities when a U-shaped narrow channel is filled with the double zero material.

To illustrate the cloaking capability we embedded an object (represented by a through-hole opening 3×4 units in size) within the DZIM metamaterial. The opening had clamped boundary conditions. The remaining conditions were unchanged with respect to the case discussed above. The numerical results (Fig.6b) show that the wave emerges on the opposite side of the slab being completely unaffected. Comparing these results with Fig.6a, we see that the acoustic field downstream of the scatterer does not carry any information about the scatterer itself therefore confirming the cloaking capability of the medium.

In a similar way, we tested the transmission performance of a U-shaped waveguide channel. The change in cross section was operated within the double-zero-index slab by shrinking the middle section from 10 to 4 units. Similarly to the cloaking case, clamped boundary conditions were imposed on all the walls of the U-shaped waveguide while the remaining boundaries were left free. In addition, perfectly matched layers were used on the top and bottom surfaces to absorb the outgoing waves and eliminate reflections. We observe that the incident plane wave (A_0 mode at $f = 27.04$ kHz) propagated through the U-shaped channel completely unaffected while picking up only a minor phase distortion. Considering the large extent of the impedance discontinuity induced within the DZIM slab, this distortion is almost negligible. Figure 10 in appendix provided the contour plots in terms of amplitude and phase corresponding to the results (Fig.6b and c). In conclusions, these results confirm the ability of the proposed design to create supercoupling effects in structural waveguides.

E. Experimental Results

We performed an experimental investigation in order to validate the concept of DZIM structural waveguide. We selected the supercoupling case for testing because it is the most challenging condition to achieve and therefore the most representative of the actual performance. To facilitate fabrication and testing, we rescaled the structure by reducing the plate thickness to 0.004 m and the unit cell dimension to half of the original size. The rescaled design resulted in a Dirac-like point at 54.08 kHz. The test sample was fabricated with extended edges along the U-Shaped waveguide channel in order to be able to enforce the boundary conditions. For simplicity, instead of creating a complex setup to impose the clamped conditions used in the simulation results (Fig.6c), we decided to treat the edges of the U-section with viscoelastic damping material while clamping the remaining edges.

The torus-like tapers were CNC machined from an initially flat aluminum plate while the center masses were cut from aluminum bars and successively glued on the taper. The experimental sample was mounted vertically in an aluminum frame and viscoelastic tape was applied on the top and bottom edges in order to minimize reflections from the boundaries. An array of Micro Fiber Composite (MFC) patches (Fig.7a) was surface bonded on the plate and simultaneously actuated to generate a quasi A_0 planar incident wave. The out-of-plane response (velocity) of the entire plate was acquired using a Polytec PSV-500 laser scanning vibrometer. We performed both steady-state and transient measurements. The steady-state response was collected following a harmonic excitation at the target frequency of 54.1 kHz. The time transient measurement was obtained in response to a 50-count wave-burst excitation signal having a 54.1 kHz center frequency. Figure 7b shows the measured out-of-plane velocity field at a fixed time instant while the inset provides an enlarged view of the wave field in the area after the DZIM slab. The data in this inset were obtained from a separate time transient scan which was performed exclusively on the area following the DZIM (white dashed box in Fig.7a) by using an increased scanning mesh size (for improved resolution) and a rescaled colorbar range. Despite some unwanted reflections due to the finite size of the test sample, the planar nature of the transmitted wave field is clearly recognizable. At the same time, the transmitted intensity is subject to a substantial level of attenuation. Figure 7c and d show the amplitude and phase distribution of the steady-state response at the target frequency. Overall, the phase field distribution over the entire structure (Fig.7d) appears consistent with the numerical results (see Fig.10 in the appendix) and the planar nature of the transmitted wave fields is still well

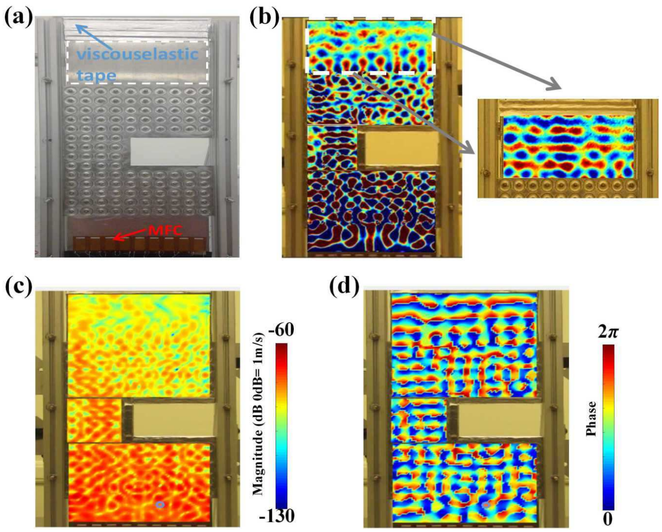

FIG. 7. Experimental setup and results. (a) Front view of the testbed consisting of a $4mm$ thick aluminum plate with a U-shaped waveguide channel filled with DZIM material. An array of MFC patches was surface bonded to generate the ultrasonic excitation. The scans covered the entire plate including the DZIM section where the out-of-plane velocity response was measured. (b) The measured transmitted A_0 wave field (out-of-plane velocity) showing that the waves propagates through the U-shaped channel preserving its planar nature. The inset shows an enlarged view of the wave field after the DZIM section (marked by the white dashed box). This data was obtained by performing a separate time transient scan that employed a refined scanning mesh grid and a rescaled colorbar range. (c) and (d) show the amplitude and phase distribution of the steady-state responses of the whole structure at the targeted frequency.

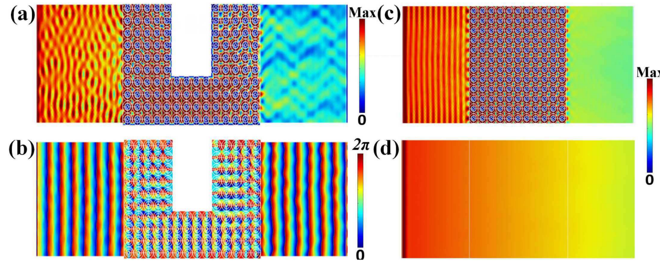

FIG. 8. Numerical simulations showing the effect of damping in a DZIM material. (a) and (b) show the phase and amplitude distributions of the wave field for the supercoupling case when a loss factor $\eta_s = 0.01$ is added to the whole structure. Comparisons of the amplitude attenuation level obtained in identical damped waveguides with (c) and without DZIM (d) are also presented. A significant amplification of the attenuation level can be observed clearly.

identifiable. Similarly, the amplitude field distribution (Fig.7c) highlights the attenuation in the intensity as the wave is transmitted through the DZIM section.

To further understand the origin of the large attenuation of the transmitted amplitude, we performed additional numerical analysis by taking into account the effect of damping. Aluminum has a small intrinsic loss factor that can vary depending on the specific type of alloy and manufacturing treatments but that generally never exceed $\eta_s = 0.01$. Hence, we added this loss factor to the whole structure by using a complex notation of the Young's modulus $E = E_0(1 + \eta_s j)$. The amplitude and phase distribution of the wavefield for the case of supercoupling were recalculated and the results are provided in Fig.8a and b. These results are in much better agreement with the experimental observations therefore confirming the limited effect of damping on the phase distribution and the large impact on the amplitude attenuation. Given the large observed attenuation, somewhat beyond the expected amplitude reduction due to a $\eta_s = 0.01$, we performed an additional numerical analysis on a flat plate with a comparable value of damping. The results (Fig.8c and d) show that a much lower level of attenuation should be expected when the DZIM is not present. This comparison suggests that the DZIM produces also a significant amplification of the damping effect. These results are consistent with recent experimental studies [63, 64] on locally resonant acoustic metamaterials that demonstrated how losses, even in a small amount, might have a strong impact on the dynamic response. Nevertheless, further theoretical analyses would be required to rigorously assess this attenuation amplification mechanism in presence of double-zero material properties.

Overall, the measurements confirm the theoretical and numerical predictions by clearly indicating that the A_0 mode can be propagated undistorted through the U-shaped DZIM waveguide channel. Nevertheless, significant amplitude attenuation takes place during the transmission which is in general not due to backscattering but due to an enhanced effect of damping.

III. CONCLUSIONS

We have presented and experimentally demonstrated the design of a double-zero-index structural waveguide able to achieve simultaneous zero effective density and elastic compliance. The design leverages locally-resonant geometric tapers that are used as fundamental unit cells to achieve and tune Dirac-like dispersion at the center of the Brillouin zone. We showed, both by theoretical and numerical methods, that the material can be mapped to a double zero effective medium when excited in the neighborhood of the Dirac-like point. Full field numerical simulations showed that this material can be used to achieve cloaking and supercoupling in elastic waveguides. Both theoretical and numerical results were confirmed by experimental measurements that validated the design and provided conclusive evidence that double zero properties can be successfully achieved in solids. This study also highlighted the important role of damping when locally-resonant materials are excited in proximity of zero effective density conditions. While the phase profile are not altered, the amplitude of the transmitted wave can suffer a severe reduction.

IV. ACKNOWLEDGMENTS

The authors gratefully acknowledge the financial support of the Air Force Office of Scientific Research under the grant YIP FA9550-15-1-0133.

---

[1] R. V. Craster and S. Guenneau, *Acoustic Metamaterials: Negative Refraction, Imaging, Lensing and Cloaking* (Heidelberg: Springer, 2012).

[2] P. A. Deymier, *Acoustic metamaterials and phononic crystals* (Heidelberg: Springer, 2013).

[3] V. G. Veselago, "The electrodynamics of substances with simultaneously negative values of ϵ and μ," Sov.Phys. Usp. **10**, 509–514 (1968).

[4] J. B. Pendry, "Negative refraction makes a perfect lens," Physical Review Letter **85**, 3966 – 3975 (2000).

[5] D. R. Smith, "Composite medium with simultaneously negative permeability and permittivity," Phys. Rev. Lett. **84**, 4184–4187 (2003).

[6] D. R. Smith, "Experimental verification of a negative index of refraction," Science **292**, 77–79 (2001).

[7] M. S. Kushwaha, P. Halevi, L. Dobrzynski, and B. Djafari-Rouhani, "Acoustic band structure of periodic elastic composites," Phys. Rev. Lett. **71**, 2022–2025 (1993).

[8] F. R. Montero de Espinosa, E. Jiménez, and M. Torres, "Ultrasonic band gap in a periodic two-dimensional composite," Phys. Rev. Lett. **80**, 1208–1211 (1998).

[9] S. Yang, J.H. Page, Z. Liu, M.L. Cowan, C.T. Chan, and P. Sheng, "Ultrasound tunneling through 3d phononic crystals," Phys. Rev. Lett. **88**, 1043011 – 1043014 (2002).

[10] H. Sanchis-Alepuz, Y. A. Kosevich, and J. Sanchez-Dehesa, "Acoustic analogue of electronic bloch oscillations and resonant zener tunneling in ultrasonic superlattices," Phys. Rev. Lett. **98**, 134301 (2007).

[11] D. Garcia-Pablos, M. Sigalas, F.R. Montero de Espinosa, M. Torres, M. Kafesaki, and N. Garcia, "Theory and experiments on elastic band gaps," Phys. Rev. Lett. **84**, 4349 (2000).

[12] J.O. Vasseur, P.A. Deymier, B. Chenni, B. Djafari-Rouhani, L. Dobrzynski, and D. Prevost, "Experimental and theoretical evidence for the existence of absolute acoustic band gaps in two-dimensional solid phononic crystals," Phys. Rev. Lett. **86**, 3012 (2001).

[13] S. Zhang, L. Yin, and N. Fang, "Focusing ultrasound with an acoustic metamaterial network," Phys. Rev. Lett. **102**, 194301 (2009).

[14] G. Lerosey, J. de Rosny, and M. Tourin, A.and Fink, "Focusing beyond the diffraction limit with far-field time reversal," Science.

[15] R. Abasi, L. Markley, and G.V. Eleftheriades, "Experimental verification of subwavelength acoustic focusing using a near-field array of closely spaced elements," J. Acoust. Soc. Am. **130**, 405 (2011).

[16] Y. Li, B. Liang, X. Tao, X. Zhu, X. Zou, and J. Cheng, "Acoustic focusing by coiling up space," Appl. Phys. Lett. **101**, 233508 (2012).

[17] H. Zhu and F. Semperlotti, "Metamaterial based embedded acoustic filters for structural applications," AIP Advances **3**, 092121 (2013).

[18] Z. He, Y. Heng, S. Peng, Y. Ding, M. Ke, and Z. Liu, "Acoustic collimating beams by negative refraction in two-dimensional phononic crystal," J. Appl. Phys. **105**, 116105 (2009).

[19] O.A. Kaya, A. Cicek, and B. Ulug, "Self-collimated slow sound in sonic crystals," J. Phys. D, Appl. Phys. **45**, 365101 (2012).

[20] J. Mei, B. Hou, M. Ke, S. Peng, H. Jia, Z. Liu, J. Shi, W. Wen, and P. Sheng, "Acoustic wave transmission through a bull's eye structure," Appl. Phys. Lett. **92**, 124106 (2008).

[21] J. J. Park, C. M. Park, K. J. B. Lee, and S. H. Lee, "Acoustic superlens using membrane-based metamaterials," Appl. Phys. Lett. **106**, 051901 (2015).

[22] J. Christensen and F. J. Garca de Abajo, "Acoustic field enhancement and subwavelength imaging by coupling to slab waveguide modes," Appl. Phys. Lett. **97**, 164103 (2010).

[23] J. Li, L. Fok, X. Yin, G. Bartal, and X. Zhang, "Experimental demonstration of an acoustic magnifying hyperlens," Nat. Mat. **8**, 931 (2009).

[24] F. Semperlotti and H. Zhu, "Achieving selective damage interrogation and sub-wavelength resolution in thin plates with embedded metamaterial acoustic lenses," J. Appl. Phys. **116**, 054906 (2014).

[25] M. Ambati, N. Fang, C. Sun, and X. Zhang, "Surface resonant states and superlensing in acoustic metamaterials," Phys. Rev. B **75**, 195447 (2007).

[26] C. M. Park, J. J. Park, S. H. Lee, Y. M. Seo, C. K. Kim, and S. H. Lee, "Amplification of acoustic evanescent waves using metamaterial slabs," Phys. Rev. Lett. **107**, 194301 (2011).

[27] B. Morvan, A. Tinel, A.-C. Hladky-Hennion, J. Vasseur, and B. Dubus, "Experimental demonstration of the negative refraction of a transverse elastic wave in a two-dimensional solid phononic crystal," Appl. Phys. Lett. **96**, 101905 (2010).

[28] J. Pierre, O. Boyko, L. Belliard, J.O. Vasseur, and B. Bonello, "Negative refraction of zero order flexural lamb waves through a two-dimensional phononic crystal," Appl. Phys. Lett. **97** (2010).

[29] N. Kaina, F. Lemoult, M. Fink, and G. Lerosey, "Negative refractive index and acoustic superlens from multiple scattering in single negative metamaterials," Nature **525**, 77 (2015).

[30] V. M. García-Chocano, J. Christensen, and José Sánchez-Dehesa, "Negative refraction and energy funneling by hyperbolic materials: An experimental demonstration in acoustics," Phys. Rev. Lett. **112**, 144301 (2014).

[31] A. Alù, M. G. Silveirinha, A. Salandrino, and N. Engheta, "Epsilon-near-zero metamaterials and electromagnetic sources: Tailoring the radiation phase pattern," Phys. Rev. B **75**, 155410 (2007).

[32] S.N Enoch, G. Tayeb, P. Sabouroux, N. Guérin, and P. Vincent, "A metamaterial for directive emission,"

Phys. Rev. Lett. **89**, 213902 (2002).

[33] A. Alu, F. Bilotti, N. Engheta, and L. Vegni, "Metamaterial covers over a small aperture," IEEE Transactions on Antennas and Propagation **54**, 1632–1643 (2006).

[34] J. C. Soric, N. Engheta, S. Maci, and A. Alu, "Omnidirectional metamaterial antennas based on *varepsilon*-near-zero channel matching," IEEE Transactions on Antennas and Propagation **61**, 33 (2013).

[35] R. W. Ziolkowski, "Propagation in and scattering from a matched metamaterial having a zero index of refraction," Phys. Rev. E **70**, 046608 (2004).

[36] M. Silveirinha and N. Engheta, "Tunneling of electromagnetic energy through subwavelength channels and bends using ϵ-near-zero materials," Phys. Rev. Lett. **97**, 157403 (2006).

[37] M. Silveirinha and N. Engheta, "Design of matched zero-index metamaterials using nonmagnetic inclusions in epsilon-near-zero media," Phys. Rev. B **75**, 075119 (2007).

[38] D. C. Adams, S. Inampudi, T. Ribaudo, D. Slocum, S. Vangala, N. A. Kuhta, W. D. Goodhue, V. A. Podolskiy, and D. Wasserman, "Funneling light through a subwavelength aperture with epsilon-near-zero materials," Phys. Rev. Lett. **107**, 133901 (2011).

[39] M. G. Silveirinha and N. Engheta, "Transporting an image through a subwavelength hole," Phys. Rev. Lett. **102**, 103902 (2009).

[40] G. V. Naik, J. Kim, and A. Boltasseva, "Oxides and nitrides as alternative plasmonic materials in the optical range," Opt. Mater. Express **1**, 1090–1099 (2011).

[41] R. Fleury and A. Alù, "Extraordinary sound transmission through density-near-zero ultranarrow channels," Phys. Rev. Lett. **111**, 055501 (2013).

[42] L. Zheng, Y. Wu, X. Ni, Z. Chen, M. Lu, and Y. Chen, "Acoustic cloaking by a near-zero-index phononic crystal," Appl. Phys. Lett. **104**, 161904 (2014).

[43] X. Xu, P. Li, X. Zhou, and G. Hu, "Experimental study on acoustic subwavelength imaging based on zero-mass metamaterials," Europhysics Letters **109**, 28001 (2015).

[44] F. Liu, Y. Lai, X. Huang, and C. T. Chan, "Dirac cones at k=0 in phononic crystals," Phys. Rev. B **84**, 224113 (2011).

[45] T.C. Wu, Y. Lai, Z. H. Hang, H. Zheng, and C.T. Chan, "Dirac cones induced by accidental degeneracy in photonic crystals and zero-refractive-index materials," Nat. Mater. **10**, 582 (2011).

[46] F. Liu, X. Huang, and C.T. Chan, "Dirac cones at $k = 0$ in acoustic crystals and zero refractive index acoustic materials," Appl. Phys. Lett. **100**, 071911 (2012).

[47] Y. Li, S. Kita, P. Muoz, O. Reshef, D. I. Vulis, M. Yin, M. Lonar, and E. Mazur, "Realization of an all-dielectric zero-index optical metamaterial," Nat. Photonics **7**, 791 (2013).

[48] P. Moitra, Y. Yang, Z. Anderson, I. I. Kravchenko, D. P. Briggs, and J. Valentine, "On-chip zero-index metamaterials," Nat. Photonics **9**, 738 (2015).

[49] S. Wu and J. Mei, "Flat band degeneracy and near-zero refractive index materials in acoustic crystals," AIP Advances **6**, 015204 (2016).

[50] M. W. Ashraf and M. Faryad, "On the mapping of dirac-like cone dispersion in dielectric photonic crystals to an effective zero-index medium," J. Opt. Soc. Am. B: Opt. Phys. **33**, 1008 (2016).

[51] F. Liu, F. Zhang, W. Wei, N. Hu, G. Deng, and Z. Wang, "Scattering of waves by three-dimensional obstacles in elastic metamaterials with zero index," Phys. Rev. B **94**, 224102 (2016).

[52] H. Zhu and F. Semperlotti, "Phononic thin plates with embedded acoustic black holes," Phys. Rev. B **91**, 104304 (2015).

[53] H. Zhu and F. Semperlotti, "Anomalous refraction of acoustic guided waves in solids with geometrically tapered metasurfaces," Phys. Rev. Lett. **117**, 034302 (2016).

[54] H. Zhu and F. Semperlotti, "Two-dimensional structure-embedded acoustic lenses based on periodic acoustic black holes," arXiv preprint arXiv:1701.03445 (2017).

[55] J. Mei, Y. Wu, C. T. Chan, and Z. Q. Zhang, "First-principles study of dirac and dirac-like cones in phononic and photonic crystals," Phys. Rev. B **86**, 035141 (2012).

[56] M. Willatzen and Lok C. Lew Yan Voon, *The k·p Method: Electronic Properties of Semiconductors* (Springer, 2009).

[57] Z. Hou and B. M. Assouar, "Modeling of lamb wave propagation in plate with two-dimensional phononic crystal layer coated on uniform substrate using plane-wave-expansion method," Phys. Lett. A **372**, 2091 (2008).

[58] Y. Lai, Y. Wu, P. Sheng, and Z. Zhang, "Hybrid elastic solids," Nat. Mat. **10**, 620–624 (2011).

[59] R. V. Craster, J. Kaplunov, and A. V. Pichugin, "High-frequency homogenization for periodic media," Proceedings of the Royal Society of London A: Mathematical, Physical and Engineering Sciences **466**, 2341–2362 (2010).

[60] R. V. Craster, J. Kaplunov, E. Nolde, and S. Guenneau, "High-frequency homogenization for checkerboard structures: defect modes, ultrarefraction, and all-angle negative refraction," J. Opt. Soc. Am. A **28**, 1032–1040 (2011).

[61] Y. Ding, Z. Liu, C. Qiu, and J. Shi, "Metamaterial with simultaneously negative bulk modulus and mass density," Phys. Rev. Lett. **99**, 093904 (2007).

[62] Y. Wu, Y. Lai, and Z. Zhang, "Effective medium theory for elastic metamaterials in two dimensions," Phys. Rev. B **76**, 205313 (2007).

[63] M. Molern, M. Serra-Garcia, and C. Daraio, "Visco-thermal effects in acoustic metamaterials: from total transmission to total reflection and high absorption," New J. Phys. **18**, 033003 (2016).

[64] V. C. Henríquez, V. M. García-Chocano, and J. Sánchez-Dehesa, "Viscothermal losses in double-negative acoustic metamaterials," Phys. Rev. Applied **8**, 014029 (2017).

Appendix A: Appendix

1. Details on numerical simulations and experimental setup.

The full-wave simulations performed throughout the paper were obtained using a commercial finite element solver (COMSOL Multiphysics). The thin plate was built out of aluminum with the following properties: Young's modulus $E = 70$ GPa, density $\rho = 2700\ kg/m^3$, and Poisson's ratio $\nu = 0.33$. Perfectly matched layers were used on the outer boundaries to avoid reflections. For what concerns the experimental setup, additional details are provided here below. The experimental sample was mounted in an aluminum frame providing clamped-free boundary conditions. A 3M viscoelastic tape (3M 2552 Damping Foil Tape) was used all around the panel to minimize the effect of boundary reflections. An array of nine Micro Fiber Composite (MFC) patches was surface bonded on the plate and simultaneously actuated to generate an A_0 (quasi-) planar incident wave. The actual plate used in the experimental setup is shown in Fig.9a. The main difference with the numerical model consists in extended edges of the U-shaped section (marked by the dashed areas) that were used to enforce clamped boundaries. Numerical simulations (Fig.9b) indicated that this modification of the boundary conditions did not alter the overall behavior of the DZIM channel with respect to the original all-clamped boundary.

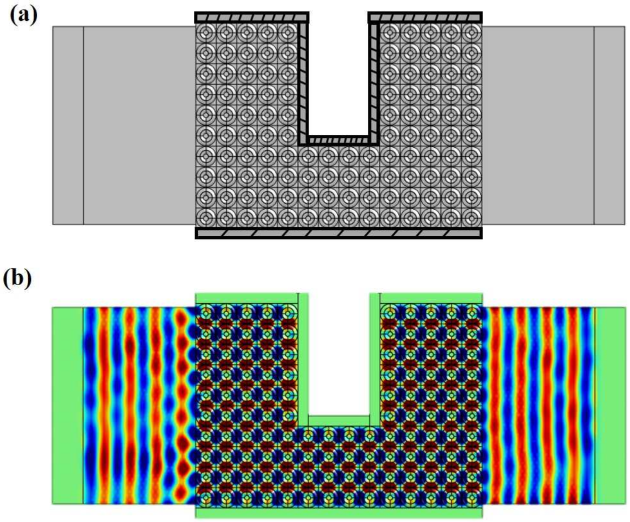

FIG. 9. (a) Schematic view of the experimental testbed. The edges of the DZIM slab (indicated by the dark dashed areas) were extended in order to allow for clamping. (b) Full field numerical simulations show that the planar wavefront of the transmitted wave is practically unaffected.

2. Details on the derivation of equation (6)

Here below we provide the detailed expression of the elements in Eqn.(6) for our 3D bulk medium. Note that, the spatial distribution of the material properties $\rho(\vec{r})$, $\lambda(\vec{r})$, and $\mu(\vec{r})$ is described by step functions. The gradient of these functions generates Dirac delta functions, i.e. $\nabla\lambda(\vec{r}) = \lambda_0\delta(\vec{r} = \vec{r}_0)\vec{n}$, where $\vec{r}_0$ stands for the interface between the vacuum layer and the aluminum plate and $\vec{n}$ is the normal to the interface pointing towards the aluminum domain. By substituting into Eqn. (6), the x component of $\vec{p}_{jl}$ is,

$$\begin{aligned} p_{x_{jl}} = \Bigg\{ \int_{unitcell} \Big[&(\lambda_0+\mu_0)(\frac{\partial u_{j0}}{\partial x} + \frac{\partial v_{j0}}{\partial y} + \frac{\partial w_{j0}}{\partial z}) * u_{l0}^* \\ &+ (\lambda_0+\mu_0)(\frac{\partial u_{j0}}{\partial x} * u_{l0}^* + \frac{\partial u_{j0}}{\partial y} * v_{l0}^* + \frac{\partial u_{j0}}{\partial z} * w_{l0}^*) \\ &+ 2\mu_0(\frac{\partial u_{j0}}{\partial x} * u_{l0}^* + \frac{\partial v_{j0}}{\partial x} * v_{l0}^* + \frac{\partial w_{j0}}{\partial x} * w_{l0}^*) \Big] dV \\ &+ \oint_{interface} \Big[\lambda_0 u_{j0} * (n_x u_{l0}^* + n_y v_{l0}^* + n_z w_{l0}^*) + \\ \mu_0(n_y v_{j0} * u_{l0}^* &+ n_z w_{j0} * u_{l0}^* - n_x v_{j0} * v_{l0}^* - n_x w_{j0} * w_{l0}^*) \\ &+ 2\mu_0 n_x (u_{j0} * u_{l0}^* + v_{j0} * v_{l0}^* + w_{j0} * w_{l0}^*) \Big] dA \Bigg\} \frac{(2\pi)^3}{V} \end{aligned} \tag{A1}$$

while the y component is,

$$\begin{aligned} p_{y_{jl}} = \Bigg\{ \int_{unitcell} \Big[&(\lambda_0+\mu_0)(\frac{\partial u_{j0}}{\partial x} + \frac{\partial v_{j0}}{\partial y} + \frac{\partial w_{j0}}{\partial z}) * v_{l0}^* \\ &+ (\lambda_0+\mu_0)(\frac{\partial v_{j0}}{\partial x} * u_{l0}^* + \frac{\partial v_{j0}}{\partial y} * v_{l0}^* + \frac{\partial v_{j0}}{\partial z} * w_{l0}^*) \\ &+ 2\mu_0(\frac{\partial u_{j0}}{\partial y} * u_{l0}^* + \frac{\partial v_{j0}}{\partial y} * v_{l0}^* + \frac{\partial w_{j0}}{\partial y} * w_{l0}^*) \Big] dV \\ &+ \oint_{interface} \Big[\lambda_0 v_{j0} * (n_x u_{l0}^* + n_y v_{l0}^* + n_z w_{l0}^*) + \\ \mu_0(n_x u_{j0} * v_{l0}^* &+ n_z w_{j0} * v_{l0}^* - n_y u_{j0} * u_{l0}^* - n_y w_{j0} * w_{l0}^*) \\ &+ 2\mu_0 n_y (u_{j0} * u_{l0}^* + v_{j0} * v_{l0}^* + w_{j0} * w_{l0}^*) \Big] dA \Bigg\} \frac{(2\pi)^3}{V} \end{aligned} \tag{A2}$$

The numerical values of the elements of $\vec{p}_{jl}$ can be obtained by performing numerical integrations based on the knowledge of the Bloch states.

3. Amplitude and phase distribution contours

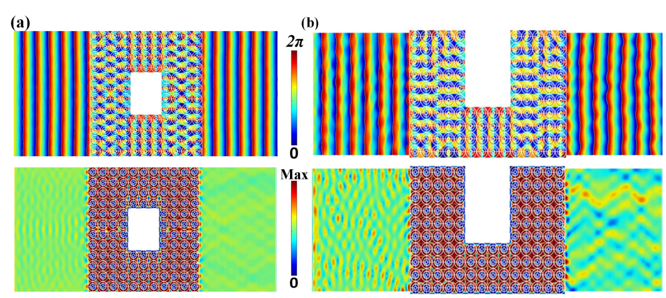

FIG. 10. Amplitude and phase distribution of the wave field for the (a) cloaking and (b) supercoupling effects illustrated in Fig.6.